RSC Advances

PAPER

View Article Online
View Journal | View Issue

Cite this: *RSC Adv.*, 2023, **13**, 6668

Magnetic properties and rare earth element diffusion behavior of hot-deformed nanocrystalline dual-main-phase Nd–Ce–Fe–B magnets

Wenbing Fan, Bang Zhou, Jiayi He, Xuefeng Liao, Yaxiang Wu, Hongya Yu, Jiangxiong Wei and Zhongwu Liu *

To inhibit the magnetic dilution effect of Ce in Nd–Ce–Fe–B magnets, a dual-alloy method is employed to prepare hot-deformed dual-main-phase (DMP) magnets using mixed nanocrystalline Nd–Fe–B and Ce–Fe–B powders. A $REFe_2$ (1 : 2, where RE is a rare earth element) phase can only be detected when the Ce–Fe–B content exceeds 30 wt%. The lattice parameters of the $RE_2Fe_{14}B$ (2 : 14 : 1) phase exhibit non-linear variation with the increasing Ce–Fe–B content due to the mixed valence states of Ce ions. Owning to inferior intrinsic properties of $Ce_2Fe_{14}B$ compared to $Nd_2Fe_{14}B$, the magnetic properties of DMP Nd–Ce–Fe–B magnets almost decrease with the increase of Ce–Fe–B addition, but interestingly, the magnet with 10 wt% Ce–Fe–B addition exhibits an abnormally increased intrinsic coercivity H_{cj} of 1215 kA m^{-1}, together with the higher temperature coefficients of remanence ($\alpha = -0.110\%$/K) and coercivity ($\beta = -0.544\%$/K) in the temperature range of 300–400 K than the single-main-phase (SMP) Nd–Fe–B magnet with $H_{cj} = 1158$ kA m^{-1}, $\alpha = -0.117\%$/K and $\beta = -0.570\%$/K. The reason may be partly attributed to the increase of Ce^{3+} ions. Different from the Nd–Fe–B powders, the Ce–Fe–B powders in the magnet are difficult to deform into a platelet-like shape because of the lack of low melting point RE-rich phase due to the precipitation of the 1 : 2 phase. The inter-diffusion behavior between the Nd-rich region and Ce-rich region in the DMP magnets has been investigated by microstructure analysis. The significant diffusion of Nd and Ce into Ce-rich and Nd-rich grain boundary phases, respectively, was demonstrated. At the same time, Ce prefers to stay in the surface layer of Nd-based 2 : 14 : 1 grains, but less Nd diffuses into Ce-based 2 : 14 : 1 grains due to the 1 : 2 phase presented in the Ce-rich region. The modification of the Ce-rich grain boundary phase by Nd diffusion and the distribution of Nd in the Ce-rich 2 : 14 : 1 phase are beneficial for magnetic properties.

Received 29th December 2022
Accepted 13th February 2023

DOI: 10.1039/d2ra08291h

rsc.li/rsc-advances

1. Introduction

Nd–Fe–B based magnets with outstanding permanent magnetic properties have been widely employed for various industrial and household applications. The increasing demand for Nd–Fe–B based magnets has accelerated the overuse of the strategic rare earth (RE) elements including Pr, Nd, Dy, Tb, *etc.*,[1] but the high-abundance La, Ce, and Y are overstocked,[2–4] which results in an imbalance in utilization of RE resources. To fabricate cost-effective RE–Fe–B permanent magnets and efficiently utilize RE resources, the Ce-based or Ce-containing RE–Fe–B magnets have received much attention in recent years.[5–8] Although early studies have shown that the intrinsic magnetic properties of $Ce_2Fe_{14}B$ compound are inferior to those of $Nd_2Fe_{14}B$,[9–11] Ce–Fe–B based magnets are still potential candidates for the permanent magnets with hard magnetic properties higher than hard ferrites.

The recent research on Nd–Ce–Fe–B alloys has been based on melt-spun ribbons,[12,13] sintered magnets,[14,15] and hot-deformed magnets.[16–18] It is reported that, with the Ce substitution of less than 10 at%, the good squareness of hysteresis loop and strong intergranular exchange coupling could be remained for melt spun $Nd_{12-x}Ce_xFe_{82}B_6$ alloys.[13] Pathak *et al.*[19] found an abnormally increased intrinsic coercivity (H_{cj}) in the $(Nd_{1-x}Ce_x)_2Fe_{14}B$ ribbons with 20 at% Ce substitution for Nd, and the similar result has been reported by others.[20] Hussain *et al.*[12] optimized the high temperature magnetic properties of nanocrystalline $(Nd_{0.8}Ce_{0.2})_{10}Fe_{84}B_6$ alloys and found that the H_{cj} of 226 kA m^{-1} could be obtained at 400 K. For the conventional sintered magnets, great achievements have been obtained in Ce doped Nd–Fe–B magnets. The maximum energy product $(BH)_{max}$ of 224 kJ m^{-3} was successfully achieved with 40 wt% Ce substitution for other rare earths.[21] To further improve the magnetic properties of Ce-containing sintered magnets, dual-alloy method based on chemical heterogeneity between two main phases has been employed to prepared dual-main-phase (DMP) magnets. By this approach, the magnetic

School of Materials Science and Engineering, South China University of Technology, Guangzhou 510640, China. E-mail: zwliu@scut.edu.cn

dilution effect of Ce addition can be effectively inhibited.[14] On the one hand, the special chemical heterogeneity formed by the inter-diffusion of REs between Nd-rich regions and Ce-rich regions in DMP magnet is beneficial to magnetic properties. The inhomogeneous RE distribution in 2 : 14 : 1 main phase grains not only facilitates the short-range exchange coupling between edge and center of the grain, but also promotes the long-range magnetostatic interaction between the grains.[9] On the other hand, the modification of grain boundary phase is also beneficial to the hard magnetic properties.[22] Zhu *et al.*[14] obtained a $(BH)_{max}$ over 342 kJ m^{-3} in the DMP sintered $(Nd_{1-x}Ce_x)_{30}(Fe,TM)_{bal}B_1$ magnet with $x = 0.3$. The magnet also exhibited improved demagnetization curve squareness. The H_{cj} of 963 kA m^{-1} for DMP $(PrNd_{0.8}Ce_{0.2})_{31}(Fe,TM)_{68}B_1$ magnet, higher than 613 kA m^{-1} for single-main-phase (SMP) magnet with the same nominal composition, was also reported by Zhu *et al.*[23] Jin *et al.*[9,24] found the H_{cj} of 1035 kA m^{-1} and $(BH)_{max}$ of 328 kJ m^{-3} for DMP magnet with 18 wt% La–Ce, which are even higher than those of SMP magnet with 9 wt% La–Ce.

As we know, the nanocrystalline magnets prepared by hot deformation technique has great potential to achieve higher H_{cj} than sintered magnets due to its smaller grain size.[16] Therefore, hot-deformation is also a good approach for fabricate high coercivity Ce-containing magnets. However, the investigations on the hot-deformed Nd–Ce–Fe–B magnets prepared by dual-alloy method are rare so far. The element distribution characteristics and elevated temperature behavior of Ce-containing DMP magnets are still not clear. In this work, the hot-deformed DMP Nd–Ce–Fe–B magnets were prepared by dual-alloy method. Their microstructure and its effects on the magnetic properties have been investigated. In particular, the chemical heterogeneity resulted from the inter-diffusion between Nd-rich and Ce-rich alloys during hot working is studied in detail.

2. Experimental

Ce–Fe–B alloy ingots with nominal composition of $Ce_{35.39}Fe_{61.62}Ga_{0.78}Si_{1.25}B_{0.96}$ (wt%) were prepared by arc melting the mixture of Ce, Fe, Ga, Si, and Fe–B metals with purities of >99.8% under Ar atmosphere. As-cast ingots were melt-spun at 20 m s^{-1} to obtain nanocrystalline ribbons followed by crushing into powder, which is named Ce–Fe–B powder in this work. The commercial Nd–Fe–B based powders with a nominal composition of $Nd_{28.47}Pr_{0.56}Fe_{bal}B_{0.97}Co_{3.63}Al_{0.13}Nb_{0.56}Zr_{0.44}$ (wt%), simplified as Nd–Fe–B powder, were also prepared by melt spinning. The Nd–Fe–B powder was mixed with Ce–Fe–B powder with various weight percentages of 10, 20, 30, 40, and 50 wt%. The produced magnets have the compositions with 11.9 wt%, 23.4 wt%, 34.3 wt%, 44.8 wt%, and 54.9 wt% Ce substitutions for Nd and Pr, respectively. The mixed powders with particle size of 100–200 μm were hot pressed at 700 °C for 30 min under a pressure of 400 MPa followed by hot deformation at 700 °C for 60 min with ~70% height reduction. For comparison, the single powders of Nd–Fe–B and Ce–Fe–B were also prepared into the magnets by hot pressing and hot deformation.

The phase constitutions of the hot deformed magnets were characterized by X-ray diffractometer (XRD, X′ Pert Pro, PANalytical, Netherlands) with Cu-Kα radiation, from $2\theta = 20$ to 70° with a step size of 0.01° and 4 s per step. All the XRD spectra were recorded in powder form. Phase analysis was performed using the Rietveld refinement with Maud software. The microstructure was investigated by transmission electron microscope (TEM, FEI Talos F200, USA). The magnetic properties were obtained by a 5 T vibrating sample magnetometer (VSM) in the physical property measurement system (PPMS-9, Quantum Design, USA). The magnetization-temperature (*M–T*) curves of the samples were measured using the zero-field-cooling process under a magnetic field of 1000 Oe in the temperature range of 300–700 K.

3. Results and discussion

3.1 Phase constitution

The XRD patterns for the hot-deformed (HDed) Nd–Ce–Fe–B magnets prepared with various Ce–Fe–B powder contents (x = 0–100 wt%) are shown in Fig. 1(a). The main diffraction peaks of all samples are corresponding to the $RE_2Fe_{14}B$ (2 : 14 : 1) phase, indicating that the 2 : 14 : 1 phase with tetragonal structure (space group $P4_2/mnm$) has been formed in all magnets. No XRD peak for $REFe_2$ (1 : 2) phase is observed in the magnet with x = 0–30 wt%. As the Ce–Fe–B content increases to 40 wt%, the 1 : 2 phase with cubic structure (space group $Fd\bar{3}m$) can be detected. With increasing x to 50 wt%, the peaks of 1 : 2 phase become more significant. Meanwhile, the intensities of (00l) diffraction peaks, such as (004), (006), and (008), for 2 : 14 : 1 phase also decrease, indicating reduced *c*-axis crystallographic alignment of the magnets with high Ce–Fe–B addition. The content and lattice parameters of 2 : 14 : 1 and 1 : 2 phases calculated from the Rietveld refinement are presented in Table 1. The traces of metallic-RE and RE_2O_3 phase in samples are not included in the analysis. The parameters a and c of 2 : 14 : 1 phase for Nd–Fe–B ($x = 0$) and Ce–Fe–B (x = 100 wt%) are 8.805 Å, 12.181 Å and 8.743 Å, 12.072 Å, respectively, due to so-called lanthanide contraction effect. However, Table 1 shows that a and c of 2 : 14 : 1 phase increase with increasing Ce–Fe–B content when x value exceeds 20 wt%, indicating the increased lattice volume. The variation of the lattice parameters of the 2 : 14 : 1 phase can be well indicated by the shift of diffraction peaks in Fig. 1(b). Unlike Nd^{3+} with a stable valence in $Nd_2Fe_{14}B$, Ce is believed to have a mixed valence of +3.44 due to the coexistence of trivalent $4f^1$ and tetravalent $4f^0$ electronic states in $Ce_2Fe_{14}B$.[25] It is well established that the Ce valence is highly related to its steric environment. As Ce^{3+} ion has a considerably larger radius than Ce^{4+} ion, the appearance of Ce valence with 3 state (carrying one 4f electron) is expected to cause the abnormal lattice expansion of 2 : 14 : 1 phase.[26] Hence, the reason for the lattice expansion of 2 : 14 : 1 phase in the samples with Ce–Fe–B contents over 20 wt% may be attributed to the appearance of Ce^{3+} ion, and similar phenomenon has been reported previously.[26] In addition, when the Ce–Fe–B content increases from 40 wt% to 50 wt%, the mass fraction of 1 : 2 phase increases from 1.9 wt% to 2.9 wt%, accounting for 11.6% and 17.7% 1 : 2 phase in Ce–

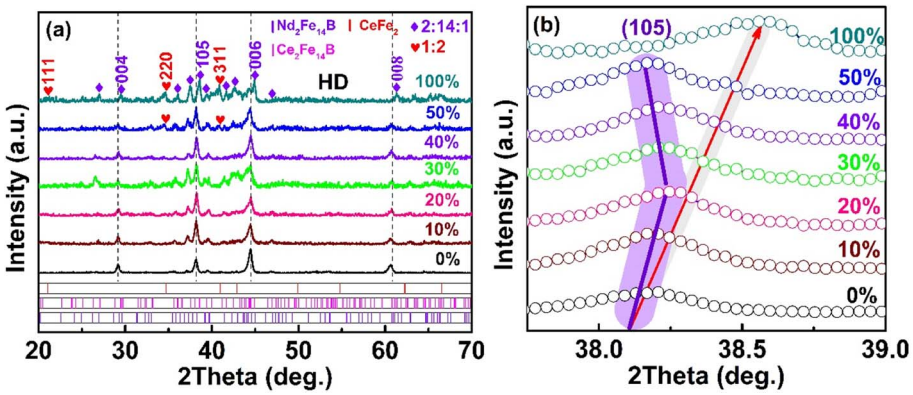

Fig. 1 XRD patterns for the hot-deformed Nd–Ce–Fe–B magnets (a) and the enlarged XRD patterns in the range of 37.8–39.0° (b) with various Ce–Fe–B contents (x = 0–100 wt%).

Table 1 Mass fraction and lattice parameters of different phases in the Nd–Ce–Fe–B magnets with various Ce–Fe–B addition determined by Rietveld refinement

	Mass fraction (wt%)		Lattice parameters (Å)			
			$RE_2Fe_{14}B$		$REFe_2$	
Ce–Fe–B content x (wt%)	$RE_2Fe_{14}B$	$REFe_2$	a	c	c/a	a
0	100	—	8.805	12.181	1.383	—
10	100	—	8.802	12.180	1.384	—
20	100	—	8.795	12.174	1.384	—
30	100	—	8.796	12.177	1.384	—
40	98.1	1.9	8.798	12.179	1.384	7.313
50	97.1	2.9	8.801	12.180	1.384	7.320
100	83.6	16.4	8.743	12.072	1.381	7.309

Fe–B magnet (16.4 wt%). It is suggested that the 1 : 2 phase is difficult to be completely inhibited in DMP Nd–Ce–Fe–B magnets.

3.2 Room temperature magnetic properties and thermal stability

Fig. 2(a) shows the demagnetization curves of the hot-deformed samples with different Ce–Fe–B contents (x = 0–50 wt%). The hysteresis loop squareness defined as μ_0H_k/μ_0H_c,[27] where μ_0H_k is the external field when the magnetization becomes 0.9 μ_0M_r, is 0.62. As the x increases to 50 wt%, the squareness decreases monotonously to 0.29. The reason may be attributed to the lower intrinsic properties of $Ce_2Fe_{14}B$ than $Nd_2Fe_{14}B$ phase and the asynchronous demagnetization process in DMP Nd–Ce–Fe–B magnets. In addition, the decreased grain orientation (Fig. 1(a)) and the microstructure difference caused by Ce–Fe–B addition may also have significant effects on the loop squareness. Fig. 2(b) shows the room temperature magnetic properties of the magnets as a function of Ce–Fe–B addition, and the detailed values are shown in Table 2. The remanence (J_r), H_{cj}, and $(BH)_{max}$ of the hot-deformed Nd–Fe–B magnet (x = 0) are 1.34 T, 1158 kA m^{-1}, and 323 kJ m^{-3}, respectively. Interestingly, the H_{cj} of the DMP magnet with 10 wt% Ce–Fe–B addition reaches 1215 kA m^{-1}, higher than that of SMP Nd–Fe–B magnet. Pei *et al.*[20] believed that this phenomenon could be related to the mixed valence of Ce. Compared with the trivalent (3^+) of Nd, Ce has the mixed valence state of 3^+ $4f^1$ and tetravalent (4^+) $4f^0$ electronic states. The increase of Ce^{3+} ion can improve the H_{cj}, since the expansion of 2 : 14 : 1 phase lattice leads to larger lattice misfit and defects which enhances the pinning effect.[28] Yan *et al.*[29] also found the abnormal increase of H_{cj} in sintered $[(Pr,Nd)_{1-x}Ce_x]_{27.5}Dy_3Al_{0.1}Cu_{0.1}Fe_{bal.}B_1$ magnet when x = 0.24. They suggested that the higher volume fraction of grain boundary layers, due to the increase of 1 : 2 phase, contribute to the enhanced coercivity. However, in this work, the melting point of 1 : 2 phase (~925 °C) is much higher than that of hot

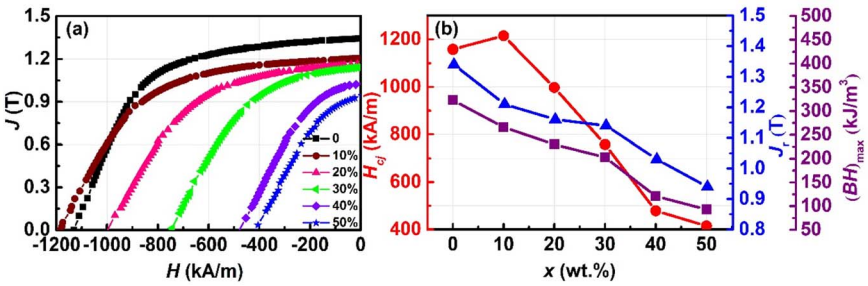

Fig. 2 The demagnetization curves (a) and magnetic properties (b) for the hot-deformed Nd–Ce–Fe–B magnets with various Ce–Fe–B contents (x = 0–50 wt%).

Table 2 Remanence J_r, coercivity H_{cj}, maximum energy product $(BH)_{max}$, magnetization under 5 T J_{5T}, temperature coefficients of remanence α and coercivity β, densities ρ of HDed Nd–Ce–Fe–B magnets with various Ce–Fe–B additions (x = 0–100 wt%)

Ce–Fe–B (x) (wt%)	J_r (T)	H_{cj} (kA m^{-1})	$(BH)_{max}$ (kJ m^{-3})	J_{5T} (T)	α (%/K)	β (%/K)	ρ (g cm^{-3})
0	1.34	1158	323	1.46	−0.117	−0.570	7.445
10	1.21	1215	266	1.37	−0.110	−0.544	7.465
20	1.16	1013	237	1.32	−0.125	−0.567	7.494
30	1.14	758	203	1.28	−0.176	−0.604	7.474
40	1.03	479	121	1.20	−0.326	−0.589	7.510
50	0.94	415	93	1.15	−0.364	−0.582	7.551
100	0.54	121	19	0.82	−0.393	−0.530	7.688

deformation temperature (~700 °C). Thus, a certain amount of 1 : 2 phase with high melting point is not beneficial to the increased coercivity in hot-deformed magnets due to the lack of wettability for smoothing the grain boundaries. It is suggested by Jin *et al.* that the chemical heterogeneity among various 2 : 14 : 1 phases caused by dual-alloy method may contribute to the excellent magnetic properties.[9] The special chemical heterogeneity results from the initial composition gradient between different two alloys. During sintering process, due to the limited inter-diffusion between two alloys, the composition of the main phase grains cannot be homogenized, leading to the chemical fluctuations of RE elements. But on the other hand, the local chemical heterogeneity in one single grain in same regions is also formed due to the high-temperature diffusion.[9] The chemical heterogeneity not only facilitates the long-range magnetostatic interaction between the grains, but also promotes the short-range exchange coupling between the core–shell region within an individual grain.[22] Therefore, the increase of Ce^{3+} ions and chemical heterogeneity among 2 : 14 : 1 grains could be responsible for the abnormal increase of H_{cj} in HDed Nd–Ce–Fe–B magnets. In addition, Fig. 2 shows that, with the addition of Ce–Fe–B, the remanence and maximum energy product decrease monotonously.

Fig. 3(a) shows the magnetization–temperature (M–T) curves of various HDed magnets. Two transition temperatures can be observed for DMP samples, which should correspond to the Curie temperatures (T_c) of 2 : 4 : 1 main phases with Ce-rich and Nd-rich compositions. The T_c of Nd-rich 2 : 14 : 1 phase roughly decreases with increasing Ce–Fe–B content, which can be explained by the increasing diffusion of Ce into Nd-rich 2 : 14 : 1 phase. In addition, the T_c of Ce-rich 2 : 14 : 1 phase for DMP samples (461–475 K) are higher than that of SMP Ce–Fe–B magnet (445 K), which indicates that Nd atoms also diffused into Ce-rich 2 : 14 : 1 phase, since the T_c of $Nd_2Fe_{14}B$ (585 K) is higher than that of $Ce_2Fe_{14}B$ (424 K). Interestingly, with increasing Ce–Fe–B content from 10 wt% to 50 wt%, the T_c of Ce-rich 2 : 14 : 1 phase has slight fluctuation, which differs from that of Nd-rich main phase. It may indicate that the diffusion of Nd into Ce-rich 2 : 14 : 1 phase is more difficult than that of Ce into Nd-rich 2 : 14 : 1 phase. The Nd concentrations in Ce-rich 2 : 14 : 1 grain have no big difference for the magnets with varied Ce–Fe–B contents.

The thermal stability of the permanent magnet is generally described by the remanence temperature coefficient (α) and coercivity temperature coefficient (β). The α and β in the temperature range T_0–T, are defined by eqn (1) and (2).[30]

$$\alpha = \frac{J_r(T) - J_r(T_0)}{J_r(T) \times (T - T_0)} \times 100\% \quad (1)$$

$$\beta = \frac{H_{ci}(T) - H_{ci}(T_0)}{H_{ci}(T) \times (T - T_0)} \times 100\% \quad (2)$$

where T_0 and T are the lowest and highest temperatures, the $J_r(T)$, $J_r(T_0)$, and $H_{ci}(T)$, $H_{ci}(T_0)$ are the remanence and coercivity at the corresponding temperatures, respectively. Fig. 3(b) show the J_r and H_{cj} as the functions of temperature for the HDed magnets with various Ce–Fe–B contents from 0 to 100%. The temperature coefficients α and β in the temperature range of 300–400 K are shown in Fig. 3(c). The values of α and β decrease from −0.110%/K to −0.364%/K and −0.544%/K to −0.582%/K, respectively, with increasing x from 10 wt% to 50 wt% (Table 2), indicating that Ce–Fe–B addition is not beneficial for the thermal stability of the remanence and coercivity. The reason can be attributed to the higher T_c of $Nd_2Fe_{14}B$ (585 K) than $Ce_2Fe_{14}B$ (424 K). The increase of H_{cj} is another reason for excellent β in Nd–Ce–Fe–B magnets with 10 wt% Ce–Fe–B addition. In addition, due to the higher β value of −0.530%/K for HDed Ce–Fe–B magnet than HDed Nd–Fe–B magnet (−0.570%/K), as shown in Table 2, the magnet with high Ce–Fe–B addition also exists good thermal stability of coercivity. Similar result could be seen from the β increases abnormally for magnets with x > 30 wt% shown in Fig. 3(c).

3.3 Microstructure and elemental diffusion behavior

In order to further understand the Ce element distribution in Nd-rich main phase, the DMP magnets have been analyzed by SEM and TEM. Fig. 4 shows the SEM (a and b), the bright field (c) and high-resolution TEM (HRTEM) images (d and e) for HDed Nd–Fe–B magnets with 30 wt% Ce–Fe–B addition. Fig. 4(a) indicates that two different grain structure regions exist in the HDed Nd–Ce–Fe–B magnet, including fine grain region and a small amount of coarse grain region. In order to clarify the difference between these two grain regions, the REs distributions were analyzed by EDS linear scanning along line 1 in Fig. 4(b), and the result are shown in Fig. 4(b) inset. The Ce content in coarse grain region is higher than that in fine grain region, while the Nd content is opposite. The results indicate

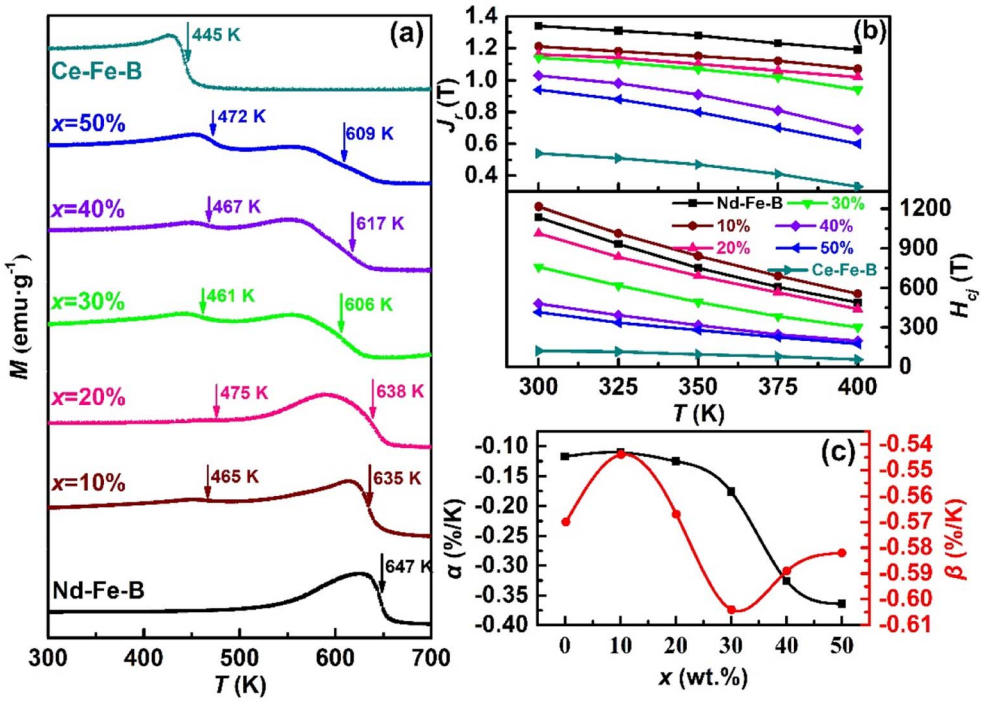

Fig. 3 *M*–*T* curves (a) for the HDed Nd–Ce–Fe–B magnets with various Ce–Fe–B contents (x = 0–100 wt%). Temperature dependent remanence and coercivity (b), and the temperature dependent temperature coefficients (c) for the HDed Nd–Ce–Fe–B magnets under the temperature range of 300–400 K.

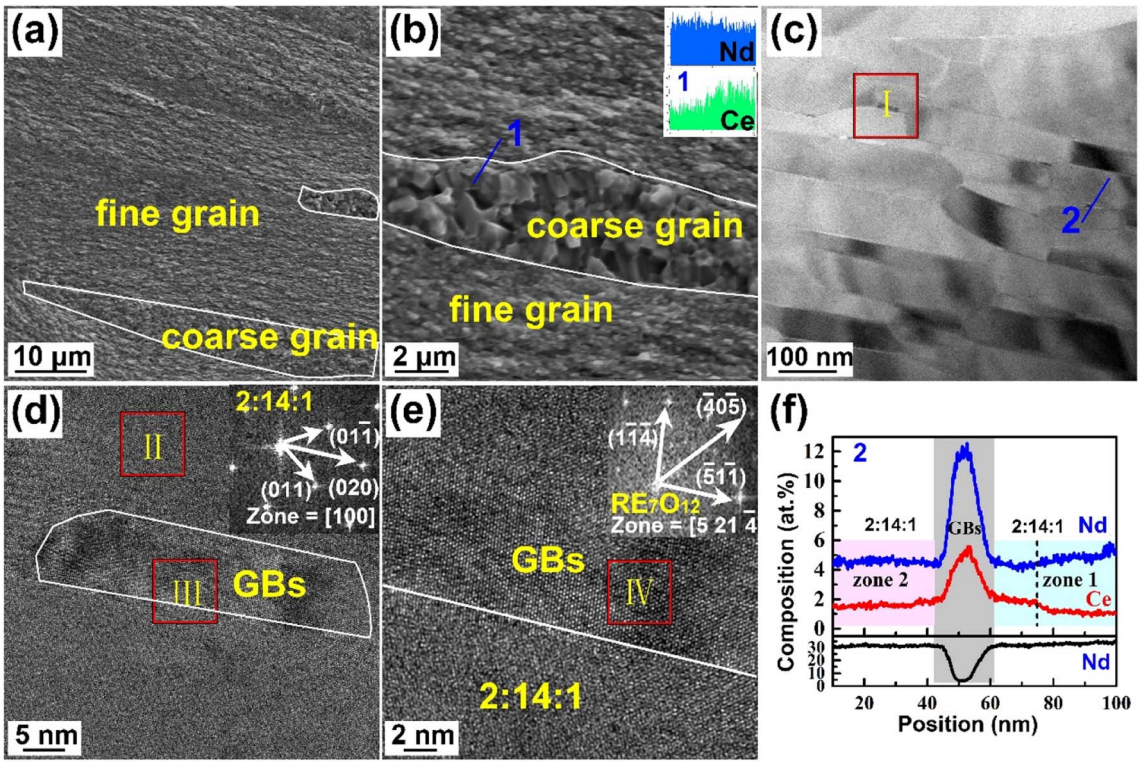

Fig. 4 The cross-sectional SEM images (a and b) and the bright field TEM image (c) for as-deformed magnets with 30 wt% Ce–Fe–B addition. The HRTEM images of region I in (c) and region III in (d) are shown in (d) and (e), respectively. The SAED (region II) and FFT (region IV) for the HRTEM images are shown in (d) and (e) insets, respectively. The inset in (b) shows the Nd and Ce distribution of EDS linear scanning (line 1 in b). The EDS line scanning (line 2) from (c) is shown in (f).

that the coarse grain region and the fine grain region are dominated by Ce–Fe–B and Nd–Fe–B grains, respectively. Fig. 4(b) also shows that the fine grains are mostly in platelet shape, caused by deformation, while the coarse grains are all equiaxed grains. The result thus indicated that the addition of Ce–Fe–B is unfavorable for the deformation of the magnet. Previously, many studies[31,32] have demonstrated that Ce–Fe–B magnet is difficult to deform due to the presence of $CeFe_2$ phase with high melting point (~925 °C). The platelet-like grains in Fig. 4(c), obtained from fine grain region, are the typical morphology of anisotropic Nd–Fe–B magnets, indicating an orientation structure of the DMP magnet. Region I in Fig. 4(c) is the grain boundary region of magnet, and corresponding HRTEM image shows in Fig. 4(d). The region II and region III in Fig. 4(d) are located at the main phase and grain boundary respectively. The selected-area electron diffraction (SAED) pattern of region II in Fig. 4(d) further identify the main phase is 2 : 14 : 1 phase. Fig. 4(e) is the HRTEM image of region III, and the grain boundary region of region IV in Fig. 4(e) shows the fast Fourier transformation (FFT) pattern that is consistent with RE_7O_{12} phase with the zone axis of [5 21 –4]. The hcp structure RE_7O_{12} phase is found in grain boundaries, and the thin grain boundary with several nanometers in width are clearly observed. The thin RE-rich phases which distributed around the 2 : 14 : 1 phase is beneficial to isolating the main phase grains. Fig. 4(f) shows the EDS scanning along line 2 across a grain boundary (GB) in Fig. 4(c). The result shows that the Ce content in RE-rich phase is significantly higher than that of 2 : 14 : 1 main phase, indicating that Ce can diffuse through the channel of grain boundary into Nd-rich main phase. With Ce diffusing from Ce–Fe–B grains to Nd–Fe–B grains, Nd also diffuses from Nd–Fe–B grains to Ce–Fe–B grains. It is worth noting that Ce element exhibits different distributions inside the different Nd-rich main phase grains, as shown in Fig. 4(f) for two grains along line 2. From the right side of the Ce concentration curve, more Ce stays in grain surface than in grain center of Nd-rich main phase. This non-uniform Ce distribution within individual Nd-rich grain indicates the chemical heterogeneity of Nd and Ce within the main phase grain, which is caused by the limited diffusion of REs. Different from the gradient Ce distribution in right side grain, the more homogeneous Ce distribution is observed in left side grain, indicating that the chemical heterogeneity of REs also exists among main phase grains. The similar elemental distribution in main phase of DMP Nd–Ce–Fe–B sintered magnets has also been reported before[9] and it is reported to be beneficial to magnetic properties.

Fig. 5 shows the STEM-EDS elemental mappings for the DMP magnet with 30 wt% Ce–Fe–B addition. The RE elements distribution in two main phase grains, grain 1 and grain 2, marked by dotted lines and solid lines, respectively, further verifies that the elemental inter-diffusion occurs in DMP magnet. Compared with the relatively homogeneous RE distribution in grain 1, the Nd and Ce in grain 2 prefers to staying in the center and surface of 2 : 14 : 1 phase, respectively. The inhomogeneous RE distribution in grain 2 is consistent with the EDS line scan result of region 1 in Fig. 4(f). Different from the sintered DMP magnet,[9] Nd–Ce and Ce–Nd core–shell structures are difficult to form in hot deformed magnet, because the lower deforming temperature which limits the REs diffusion. Unlike the distribution of RE elements, Fe and Co tend to enrich in main phase, while Ga prefers to stay at grain boundaries. The Ga with low melting point can improve the wettability of RE-rich phase,[33] promoting the inter-diffusion of RE elements.

Based on the microstructure above, the chemical inhomogeneity of Nd and Ce elements in DMP Nd–Ce–Fe–B magnet could be described in Fig. 6. Two kinds of 2 : 14 : 1 phase grain with different deformation ratios, *i.e.* platelet shaped grains and equiaxed grains, exist in DMP Nd–Ce–Fe–B magnet. In general, the deformation ability is great affected by the low melting point RE-rich grain boundary phase. It has been found that Ce–Fe–B alloys are difficult to deform due to the lack of low melting point grain boundary phase since the excessive Ce is consumed by the formation of high melting point 1 : 2 phase (~925 °C).[32] Hence, the platelet-like grains in the microstructure are Nd-rich main phase and the equiaxed-like grains that are hard to deform are Ce-rich main phase. The formation of 1 : 2 phase not only reduces the RE-rich grain boundary layers required for H_{cj},[34] but also decreases the J_r by introducing the non-ferromagnetic phase.[35] The elemental inter-diffusion between Nd–Fe–B and

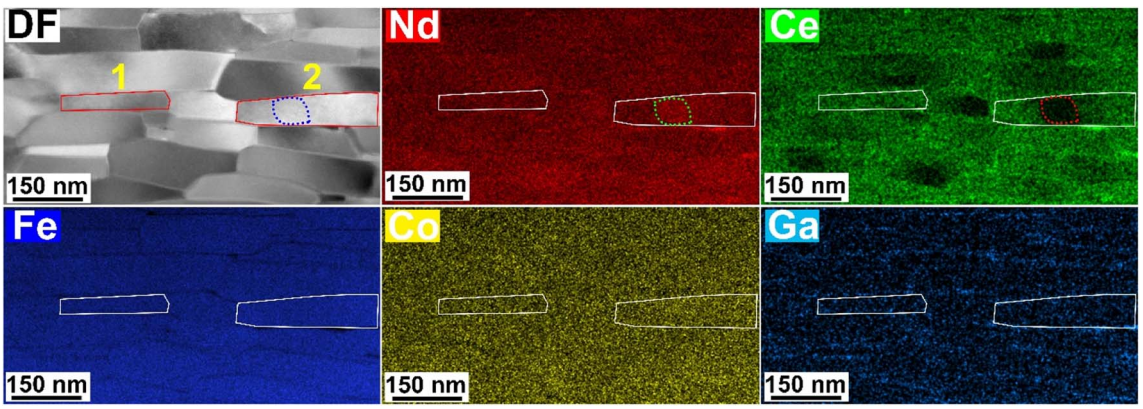

Fig. 5 The STEM-EDS elemental mappings for as-deformed magnet with 30 wt% Ce–Fe–B addition.

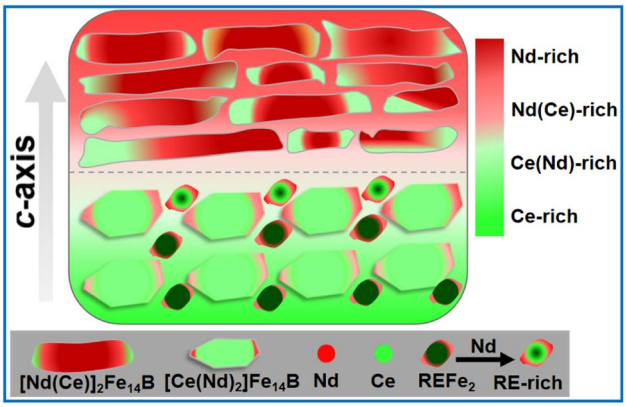

Fig. 6 The chemical inhomogeneity construction in hot-deformed DMP Nd–Ce–Fe–B magnets.

Ce–Fe–B powders under hot pressing and hot deformation process is the main reason for chemical inhomogeneity. During hot pressing and hot deformation, the RE elements can diffuse along RE-rich phase in the grain boundary. As a result, a large amount of Nd and Ce existed in Ce-rich and Nd-rich grain boundary phase, respectively. In Ce-rich region, during inter-diffusion, the diffusion of Nd through Ce-rich grain boundary phase to Ce-rich 2 : 14 : 1 phase is limited due to the existence of 1 : 2 phase, which can be verified by *M*–*T* analysis results. Consequently, a few Nd diffuse into Ce-rich 2 : 14 : 1 phase, and it is beneficial for hard magnetic properties due to the higher intrinsic magnetic properties of $Nd_2Fe_{14}B$.[10] In addition, 1 : 2 phase was not observed in magnet with low Ce–Fe–B addition, which as shown in XRD analysis results, so the distribution of Nd in Ce-rich grain boundary phase is beneficial to inhibits the precipitation of 1 : 2 phase other than increases the thickness and continuity of grain boundary phases.[36] The modified grain boundary phase in Ce-rich region by Nd diffusion and the distribution of Nd in Ce-rich 2 : 14 : 1 phase are beneficial for hard magnetic properties. On the contrary, Ce prefers to diffusing into the Nd-rich 2 : 14 : 1 phase and staying at the surface layer of the grains, which may reduce the magnetic anisotropy of the hard grain, therefore, the coercivity decreases. It is suggested that the distribution of Nd in DMP Nd–Ce–Fe–B magnets may be the main reason why excellent hard magnetic properties were obtained. In addition, for the certain Ce-containing composition, the chemical heterogeneity in DMP magnets may promote the short-range exchange coupling within an individual grain and effectively enhance the remanence.[22] The similar chemical heterogeneity in DMP sintered magnets was also reported to be beneficial to inhibiting the magnetic dilution effect of Ce.[14]

4. Conclusions

A dual-alloy approach has been employed to prepare hot deformed nanocrystalline dual-main-phase Nd–Ce–Fe–B magnets. Nd–Fe–B powder was mixed with various additions of Ce–Fe–B powder followed by hot pressing and hot-deformation. The lattice parameters of the 2 : 14 : 1 phase increases abnormally with increasing Ce–Fe–B to 20 wt%. For the magnet with 10 wt% Ce–Fe–B addition, the optimal H_{cj} of 1215 kA m^{-1} and the excellent temperature coefficients ($\alpha = -0.110\%$/K and $\beta = -0.544\%$/K) in the temperature range of 300–400 K were obtained, which are higher than those of SMP Nd–Fe–B magnet ($H_{cj} = 1158$ kA m^{-1}, $\alpha = -0.117\%$/K, $\beta = -0.570\%$/K). The Ce valence shifts to the Ce^{3+} state in 2 : 14 : 1 phase is one reason for the lattice expansion and excellent comprehensive magnetic properties in HDed Nd–Ce–Fe–B magnets. The inter-diffusion behavior of rare earth elements during hot pressing and hot deformation is analyzed based on the phase constitution and microstructure characterizations. It has been found that Nd tends to diffuse from Nd-rich grains to Ce-rich grains, and Ce follows the reverse direction. The modification of the Ce-rich grain boundary phase by Nd diffusion is beneficial for the reduction of 1 : 2 phase and increases the continuity of grain boundary phase. Meanwhile, the diffusion of Nd in Ce-rich 2 : 14 : 1 phase is also beneficial to magnetic properties. In addition, Ce tends to diffuse into the surface of Nd-rich 2 : 14 : 1 phase, and the special chemical heterogeneity may be beneficial to inhibiting the magnetic dilution effect due to the strong short-range exchange coupling within an individual grain. This work provides a clear understanding of microstructure for hot deformed DMP Nd–Fe–B magnets with Ce addition.

Author contributions

Wenbing Fan: conceptualization, investigation, formal analysis, methodology, writing original draft, writing review & editing, Bang Zhou: data curation, investigation, Jiayi He: data curation, investigation, Xuefeng Liao: resources, validation, Yaxiang Wu: resources, data curation, investigation, Hongya Yu: resources, validation, Jiangxiong Wei: resources, validation, writing original draft, Zhongwu liu: conceptualization, supervision, funding acquisition.

Conflicts of interest

There are no conflicts to declare.

Acknowledgements

This work is supported by the National Natural Science Foundation of China (No. U21A2052 and No. 52071143).

References

1 S. Massari and M. Ruberti, *Resour. Policy*, 2013, **38**, 36–43.
2 Z. Y. Zhang, L. Z. Zhao, J. S. Zhang, X. C. Zhong, W. Q. Qiu, D. L. Jiao and Z. W. Liu, *Mater. Res. Express*, 2017, **4**, 086503.
3 Z. Y. Zhang, L. Z. Zhao, X. C. Zhong, D. L. Jiao and Z. W. Liu, *J. Magn. Magn. Mater.*, 2017, **441**, 429–435.
4 X. D. Fan, G. F. Ding, K. Chen, S. Guo, C. Y. You, R. J. Chen, D. Lee and A. R. Yan, *Acta Mater.*, 2018, **154**, 343–354.

5 Y. L. Huang, Z. H. Li, X. J. Ge, Z. Q. Shi, Y. H. Hou, G. P. Wang, Z. W. Liu and Z. C. Zhong, *J. Alloys Comp.*, 2019, **797**, 1133–1141.
6 J. S. Zhang, L. Z. Zhao, X. F. Liao, H. X. Zeng, D. R. Peng, H. Y. Yu, X. C. Zhong and Z. W. Liu, *Intermetallics*, 2019, **107**, 75–80.
7 J. S. Zhang, W. Li, X. F. Liao, H. Y. Yu, L. Z. Zhao, H. X. Zeng, D. R. Peng and Z. W. Liu, *J. Mater. Sci. Technol.*, 2019, **35**, 1877–1885.
8 Q. Z. Jiang and Z. C. Zhong, *J. Mater. Sci. Technol.*, 2017, **33**, 1087–1096.
9 J. Y. Jin, T. Y. Ma, Y. J. Zhang, G. H. Bai and M. Yan, *Sci. Rep.*, 2016, **6**, 32200.
10 X. F. Liao, J. S. Zhang, H. Y. Yu, X. C. Zhong, A. J. Khan, X. Zhou, H. Zhang and Z. W. Liu, *J. Mater. Sci.*, 2019, **54**, 14577–14587.
11 X. F. Liao, L. Z. Zhao, J. S. Zhang, G. Ahmed, A. J. Khan, H. X. Zeng, H. Y. Yu, X. C. Zhong, Z. W. Liu and G. Q. Zhang, *Curr. Appl. Phys.*, 2019, **19**, 733–738.
12 M. Hussain, X. F. Liao, R. Akram, G. Milyutin, M. Khan and Z. W. Liu, *J. Alloy Compd.*, 2020, **845**, 156292.
13 Z. B. Li, B. G. Shen, M. Zhang, F. X. Hu and J. R. Sun, *J. Alloy Compd.*, 2015, **628**, 325–328.
14 M. G. Zhu, W. Li, J. D. Wang, L. Y. Zheng, Y. F. Li, K. Zhang, H. B. Feng and T. Liu, *IEEE Trans. Magn.*, 2014, **50**, 1–4.
15 X. D. Fan, G. F. Ding, K. Chen, S. Guo, C. Y. You, R. J. Chen, D. Lee and A. R. Yan, *Acta Mater.*, 2018, **154**, 343–354.
16 X. Tang, S. Y. Song, J. Li, H. Sepehri-Amin, T. Ohkubo and K. Hono, *Acta Mater.*, 2020, **190**, 8–15.
17 X. Tang, H. Sepehri-Amin, M. Matsumoto, T. Ohkubo and K. Hono, *Acta Mater.*, 2019, **175**, 1–10.
18 H. J. Peng, D. B. Yu, X. Y. Bai, X. Lin, Y. J. Mao, Z. L. Wang and Y. Luo, *J. Rare Earth*, 2021, **39**, 986–992.
19 A. K. Pathak, M. Khan, K. A. Gschneidner Jr., R. W. McCallum, L. Zhou, K. Sun, M. J. Kramer and V. K. Pecharsky, *Acta Mater.*, 2016, **103**, 211–216.
20 K. Pei, X. Zhang, M. Lin and A. R. Yan, *J. Magn. Magn. Mater.*, 2016, **398**, 96–100.
21 S. X. Zhou, Y. G. Wang and R. Høier, *J. Appl. Phys.*, 1994, **75**, 6268–6270.
22 J. Y. Jin, M. Yan, Y. S. Liu, B. X. Peng and G. H. Bai, *Acta Mater.*, 2019, **169**, 248–259.
23 M. G. Zhu, R. Han, W. Li, S. L. Huang, D. W. Zheng, L. W. Song and X. N. Shi, *IEEE Trans. Magn.*, 2015, **51**, 2104604.
24 M. Yan, J. Y. Jin and T. Y. Ma, *Chin. Phys. B*, 2019, **28**, 077507.
25 T. W. Capehart, R. K. Mishra, G. P. Meisner, C. D. Fuerst and J. F. Herbst, *Appl. Phys. Lett.*, 1993, **63**, 3642–3644.
26 X. F. Liao, J. S. Zhang, W. Li, A. J. Khan, H. Y. Yu, X. C. Zhong and Z. W. Liu, *J. Alloy Compd.*, 2020, **834**, 155226.
27 X. Tang, J. Li, H. Sepehri-Amin, T. Ohkubo, K. Hioki, A. Hattori and K. Hono, *Acta Mater.*, 2021, **203**, 116479.
28 J. S. Zhang, X. F. Liao, K. Xu, J. Y. He, W. B. Fan, H. Y. Yu, X. C. Zhong and Z. W. Liu, *J. Mater. Chem. C*, 2020, **8**, 14855–14863.
29 C. J. Yan, S. Guo, R. J. Chen, D. Lee and A. R. Yan, *IEEE Trans. Magn.*, 2014, **50**, 1–5.
30 Z. W. Liu and H. A. Davies, *J. Magn. Magn. Mater.*, 2005, **290**, 1230–1233.
31 X. F. Liao, L. Z. Zhao, J. S. Zhang, K. Xu, B. Zhou, H. Y. Yu, X. F. Zhang, J. M. Greneche, A. Aubert, K. Skokov, O. Gutfleisch and Z. W. Liu, *J. Mater. Res. Technol.*, 2022, **17**, 1459–1468.
32 Y. H. Hou, Z. H. Nie, Y. F. Yao, Z. J. Wu, Q. Feng, W. Li, J. M. Luo and Y. L. Huang, *Intermetallics*, 2022, **148**, 107644.
33 S. N. Fan, G. F. Ding, X. D. Fan, Z. X. Wang, Z. H. Jin, H. C. Wu, S. Guo, B. Zheng, R. J. Chen, A. R. Yan and B. Meng, *J. Alloy Compd.*, 2022, **913**, 165263.
34 K. Hono and H. Sepehri-Amin, *Scr. Mater.*, 2012, **67**, 530–535.
35 X. Tang, H. Sepehri-Amin, T. Ohkubo, M. Yano, M. Ito, A. Kato, N. Sakuma, T. Shoji, T. Schrefl and K. Jono, *Acta Mater.*, 2018, **144**, 884–895.
36 K. Chen, S. Guo, X. D. Fan, G. F. Ding, L. Chen, R. J. Chen, D. Li and A. R. Yan, *J. Rare Earth*, 2017, **35**, 158–163.